ADVANCED MATERIALS
www.advmat.de

Confinement-Driven Inverse Domain Scaling in Polycrystalline $ErMnO_3$

Jan Schultheiß, Fei Xue, Erik Roede, Håkon W. Ånes, Frida H. Danmo, Sverre M. Selbach, Long-Qing Chen, and Dennis Meier**

The research on topological phenomena in ferroelectric materials has revolutionized the way people understand polar order. Intriguing examples are polar skyrmions, vortex/anti-vortex structures, and ferroelectric incommensurabilties, which promote emergent physical properties ranging from electric-field-controllable chirality to negative capacitance effects. Here, the impact of topologically protected vortices on the domain formation in improper ferroelectric $ErMnO_3$ polycrystals is studied, demonstrating inverted domain scaling behavior compared to classical ferroelectrics. It is observed that as the grain size increases, smaller domains are formed. Phase field simulations reveal that elastic strain fields drive the annihilation of vortex/anti-vortex pairs within the grains and individual vortices at the grain boundaries. The inversion of the domain scaling behavior has far-reaching implications, providing fundamentally new opportunities for topology-based domain engineering and the tuning of the electromechanical and dielectric performance of ferroelectrics in general.

1. Introduction

Ferroelectric materials are the backbone of many electronic components, finding applications as capacitors, energy harvesters, and actuators.[1] The rich functionality of ferroelectrics is closely linked to their domain structure, and substantial contributions to their dielectric, piezoelectric, and electromechanical responses originate from domain walls.[2] Because of the strong correlation between the domain morphology and the functional behavior, domain engineering is a powerful pathway for customizing the macroscopic performance of ferroelectrics.[3] Application of different electrode materials,[4] thickness variations,[5] and chemical doping[6] are common approaches that allow for stabilizing well-defined domain states on demand. Furthermore, strain effects are utilized to control the domains in ferroelectric single crystals and thin films, e.g., via substrate-related clamping effects[7] and microstructural engineering approaches that rely on dislocations,[8] secondary inclusions,[9] or precipitates.[10]

In polycrystals, an additional degree of freedom for microstructural engineering emerges from the 3D confinement due to finite grain size. A prominent example is the relation between the grain size, g, and the domain size, d, in $BaTiO_3$ polycrystals,[11,12] which facilitated the downscaling of multilayer ceramic capacitors. The relation follows the universal scaling law $d \sim g^m$.

Importantly, for all ferroelectrics investigated so far, the exponent m is positive, with a value of $m \approx 0.5$ for $BaTiO_3$[12] and $Pb(Zr,Ti)O_3$,[11] indicating that smaller grains develop smaller domains. The driving force for this scaling behavior is elastic strain, which can be released via the formation of ferroelastic domain walls. With decreasing grain size the strained volume fraction increases,[13] requiring more domain walls for strain compensation so that smaller domains become energetically favorable.[14]

Here, we show that negative coefficients, m, arise in polycrystalline hexagonal manganites, demonstrating an inversion of the established grain-size-dependent scaling behavior of ferroelectric domains. Our systematic study of the relation between domain and grain sizes in $ErMnO_3$ shows that, in contrast with $BaTiO_3$ and $Pb(Zr,Ti)O_3$, the ferroelectric domains become smaller with increasing grain size, scaling with $m \approx -0.1$. Using phase field simulations, we relate the unusual behavior to topologically protected structural vortices that naturally form in the ferroelectric phase of $ErMnO_3$[15] and their interaction with elastic strain fields.[16–18] Our findings reveal the importance of topological defects for the electric long-range order in ferroelectric polycrystals, enabling anomalous domain scaling behaviors and conceptually new ways for domain engineering.

2. Geometrical 3D Confinement in Polycrystalline $ErMnO_3$

Ternary hexagonal manganites, $RMnO_3$ (R = Sc, Y, In, and Dy–Lu), have been intensively studied as model system for improper ferroelectricity.[19] In contrast to proper ferroelectrics,

J. Schultheiß, E. Roede, H. W. Ånes, F. H. Danmo, S. M. Selbach, D. Meier
Department of Materials Science and Engineering
NTNU Norwegian University of Science and Technology
Høgskoleringen 1, Trondheim 7034, Norway
E-mail: jan.schultheiss@ntnu.no; dennis.meier@ntnu.no
F. Xue, L.-Q. Chen
Department of Materials Science and Engineering
The Pennsylvania State University
University Park, PA 16802, USA
The ORCID identification number(s) for the author(s) of this article can be found under https://doi.org/10.1002/adma.202203449.

DOI: 10.1002/adma.202203449

such as $LiNbO_3$, $Pb(Zr,Ti)O_3$, and $BaTiO_3$, the spontaneous polarization, P, is not the primary order parameter.[20,21] In $RMnO_3$, the polarization arises as a symmetry enforced consequence of a structurally driven phase transition and points in the direction of the hexagonal c-axis.[22,23] As a consequence, the material exhibits a large variety of unusual physical phenomena at the level of domains.[24] Intriguing examples range from domain walls with unique functional electronic properties[25–27] to topological vortex structures that have been utilized to test cosmological scaling laws.[28,29] Most of the research so far, however, focused on single crystalline systems,[30,31] whereas only a few studies were performed on polycrystalline films[32] or ceramics.[33–35] In particular, the impact of the microstructure on the ferroelectric domain distribution remains to be explored.

To systematically investigate the relation between the microstructure and domains, we adopt a processing routine previously suggested for isostructural $DyMnO_3$ and $YMnO_3$[36] and synthesize high-quality polycrystalline $ErMnO_3$ from oxide precursors with subsequent high-temperature heat treatment (more details on the processing can be found in the Supporting Information and Figure S1; micrographs of the samples are provided in Figure S2, Supporting Information). To confirm the phase purity of our samples, we perform powder X-ray diffraction (XRD) of a crushed pellet (**Figure 1**a), confirming $P6_3cm$ space group symmetry equivalent to $ErMnO_3$ single crystals.[37] Figure 1b presents the microstructure of the polycrystalline material with an average grain size of about 19.0 µm and the random orientation of the individual grains, measured by electron backscattered diffraction (EBSD, see Figure S3, Supporting Information, for details). In Figure 1c,d, piezoresponse force microscopy (PFM) images of the ferroelectric domain structure of the region presented in Figure 1b are displayed (topography images are displayed in Figure S4, Supporting Information). The PFM images obtained on samples with a thickness or ≈1 mm are recorded with a peak-to-peak voltage of 10 V at a frequency of 40.13 kHz which is comparable to the imaging parameters previously used for $ErMnO_3$ single crystals.[38,39] The PFM images display pronounced out-of-plane (Figure 1c) and in-plane (Figure 1d) contrast between the $+P$ and $-P$ domains (more details are

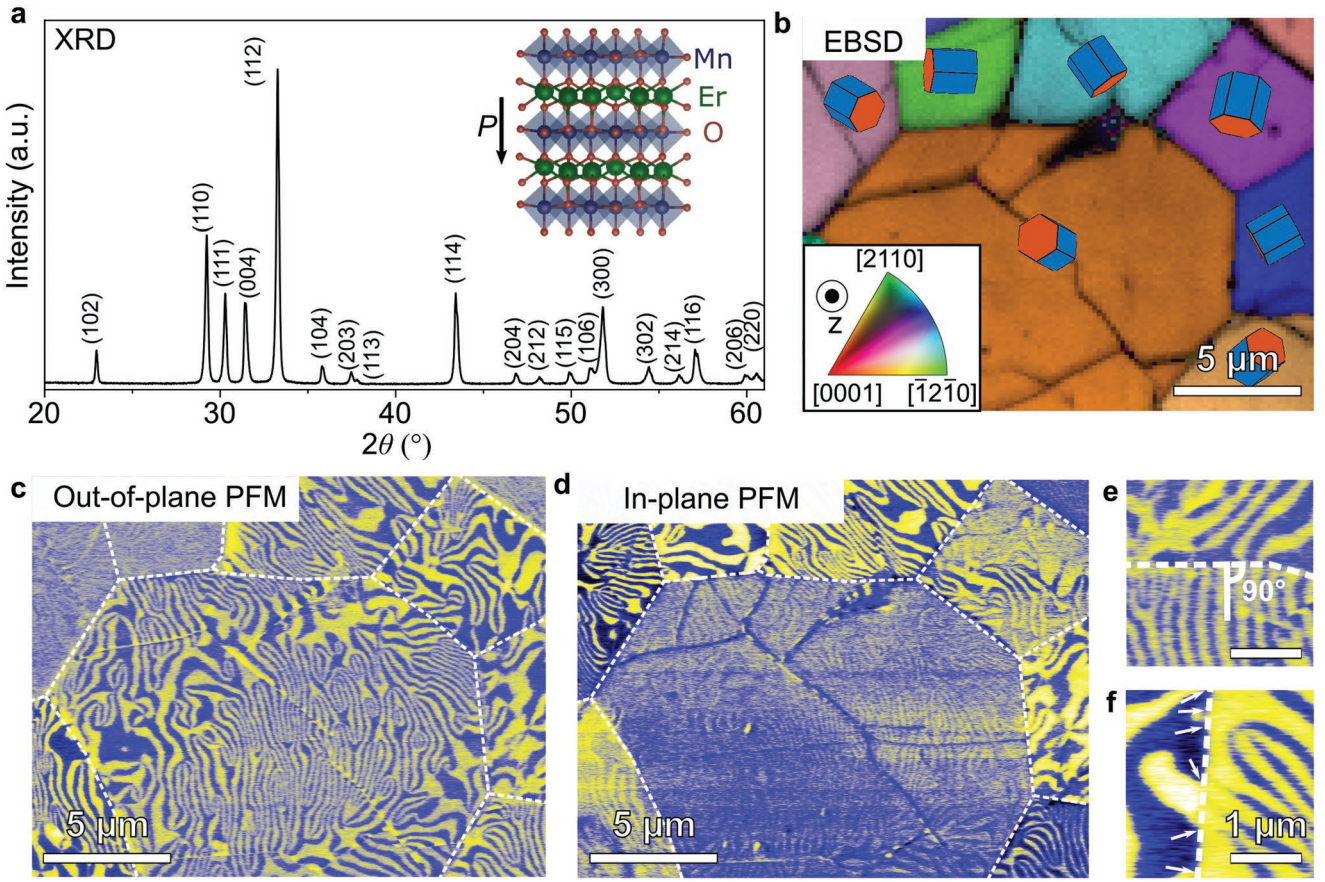

Figure 1. Structural and microstructural analysis of polycrystalline $ErMnO_3$. a) XRD pattern of crushed polycrystalline $ErMnO_3$, showing that the material has a hexagonal structure with space group symmetry $P6_3cm$. The atomic structure of the ferroelectric phase of $ErMnO_3$ with crystallographic data from ref. [37] is displayed in the inset. The direction of the spontaneous polarization vector, P, is indicated. b) EBSD results showing the orientation of the grains of the polycrystalline material indicated by blue/red hexagons. The blue surfaces represent the $(10\bar{1}0)$ and red colors the (0001) planes of the hexagonal crystal with space group $P6_3cm$. A detailed description of the fitting of the EBSD patterns is provided in Figure S3 (Supporting Information). c,d) Out-of-plane and in-plane PFM images of the same area as presented in (b). The yellow and blue regions correspond to $\pm P$ domains. The dashed white lines mark the grain boundaries. A topographic image of the investigated area is provided in Figure S4 (Supporting Information). The tendency of the domain walls to orient perpendicular to the grain boundary is highlighted in (e). The arrows in (f) highlight domain walls that do not continue over the grain boundary.

provided in Section S1.3 and Figure S5 in the Supporting Information). Within the different grains (grain boundaries are highlighted by white dashed lines) we observe the well-established domain structure of $ErMnO_3$,[25,40] which is set by the structural primary symmetry breaking order parameter at the improper ferroelectric phase transition.[23] The domain structure consists of ferroelectric 180° domains which come together in characteristic sixfold meeting points. These meeting points originate from the structural trimerization that drives the improper ferroelectric phase transition in hexagonal manganites and correspond to topologically protected vortex/anti-vortex pairs. From this, it can be inferred that the domain structure consists of the six translational domains, commonly denoted as $\alpha^{\pm}$, $\beta^{\pm}$, and $\gamma^{\pm}$ that originate from tilting of the MnO_5 bipyramids.[16,41] Although the observed domain structures are qualitatively equivalent to those found in single crystals, Figure 1c,d also reveals an important difference: Isotropic domain distributions are only observed in certain regions, whereas the majority of the investigated area exhibits elongated stripe-like domains. The patterns are reminiscent of those reported to arise in single crystals under elastic strain.[18] It was demonstrated that elastic strain drives the vortex/anti-vortex pairs into opposite directions, unfolding the domain pattern into elongated stripe-like domains.[16,17] The PFM data thus reflect nonzero strain fields within the individual grains, which are indeed expected to arise at the high-temperature improper ferroelectric phase transition of polycrystalline $ErMnO_3$.[42] Interestingly, the PFM data also reveal that domain walls have a propensity to orient perpendicular to the grain boundaries (Figure 1e) as corroborated by the statistical evaluation presented in Figure S6 (Supporting Information). The domain walls, however, do not cross the grain boundaries (Figure 1f). This behavior is fundamentally different from the ferroelectric domain structures reported for polycrystalline $BaTiO_3$[43] and $Pb(Zr,Ti)O_3$,[44] where domain walls tend to continue into neighboring grains.

This observation leads us to the conclusion that the domain structures within the different grains are largely independent of each other. This unlocks the possibility to engineer the ferroelectric domains by imposing 3D geometrical confinement via the microstructure, representing an additional degree of freedom not available in $RMnO_3$ single crystals and thin films. To confirm that the domain and domain wall behavior observed in our PFM images applies in all spatial directions and not only to the surface region, we record complementary cross-sectional images using focused ion beam (FIB) in combination with scanning electron microscopy (SEM). The respective data are presented in Figure S7 (Supporting Information), showing the same domain features as observed at the surface, that is, vortex structures which unfold into stripe-like domains toward the sub-surface grain boundaries and domain walls with a preferred orientation perpendicular to them.

3. Inverse Grain Size-Dependent Domain Scaling Behavior

In the next step, we systematically investigate the effect of 3D geometrical confinement on the domain structure by analyzing $ErMnO_3$ samples with different grain sizes manufactured using varying heat-treatment conditions as explained in the Section S1.1 in the Supporting Information. To suppress unwanted cooling-rate-dependent variations in the domain structure as studied in refs. [28,29], the cooling rate is kept constant to 5 °C min^{-1} in all manufacturing processes. SEM images (Figure S2, Supporting Information) indicate that we can readily tune the grain size in polycrystalline $ErMnO_3$ over a range of ≈1.5 to 19.0 µm using heat-treatment conditions within the temperature range of 1350–1450 °C ($T_C^{ErMnO_3}$ = 1150 °C).[28] An overview of the resulting ferroelectric domain structures for four samples with different grain sizes is presented in **Figure 2**. Analogous to the sample in Figure 1, a pronounced PFM contrast (out-of-plane) is observed for all samples showing the distribution of $\pm P$ domains. A closer inspection of the PFM data shows that polycrystalline $ErMnO_3$ samples with mean grain sizes from 4.8 to 19.0 µm develop qualitatively equivalent domain patterns, exhibiting a mixture of vortex and elongated stripe-like domains similar to those presented in Figure 1. For further reduced grain sizes, i.e., a mean grain size of 1.5 µm, the formation of a vortex- and stripe-like domain structure is suppressed as reflected by representative PFM images in Figure S8 (Supporting Information). From the evaluation of in total more than 50 grains, we find on average 0.8 ± 0.6 vortices per grain. This leads us to the conclusion that the system transitions from vortex-like to stripe-like domains, reminiscent to the unfolding of vortex domains observed in hexagonal manganite single crystals under strain.[17,18]

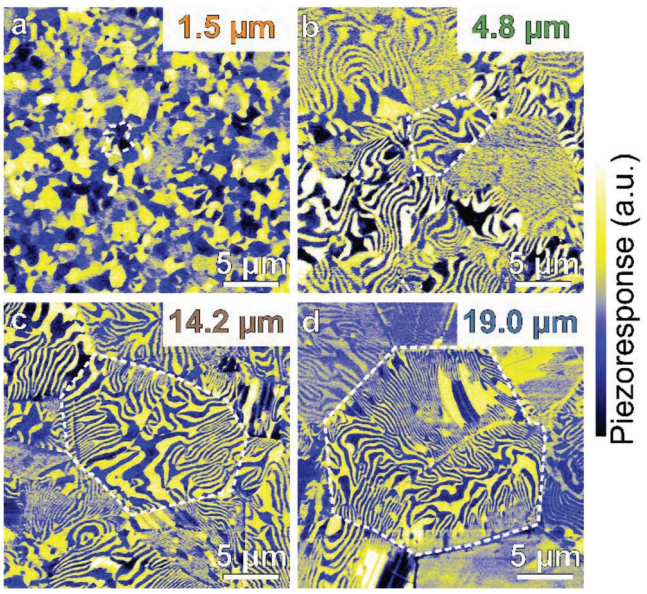

Figure 2. a–d) Domain structures observed in samples with different grain size, obtained by different heat-treatment conditions: 1350 °C, 10 min (a); 1350 °C, 4 h (b); 1400 °C, 12 h (c); 1450 °C, 12 h (d), respectively. PFM images (out-of-plane) gained with a peak-to-peak voltage of 10 V at a frequency 40.13 kHz reveal qualitatively equivalent domain patterns for mean grain sizes of 4.8, 14.2, and 19.0 µm. In contrast, for the sample with a mean grain size of 1.5 µm the vortex and stripe-like domain formation is suppressed. For each PFM image, the grain boundaries of one representative grain are highlighted by white dashed lines. SEM images of the samples with different grain sizes are displayed in Figure S2 (Supporting Information).

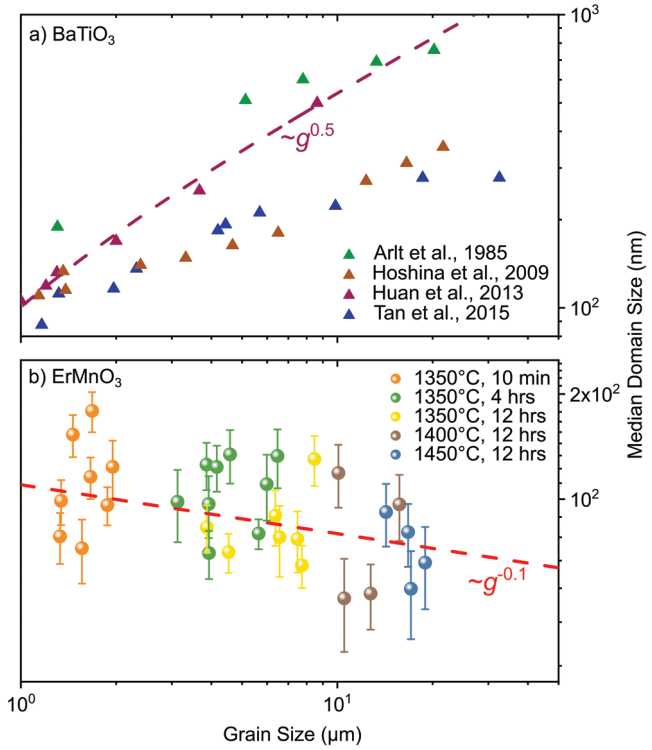

Figure 3. Grain size dependence of the domain size in polycrystalline $BaTiO_3$ and $ErMnO_3$. a) The grain size dependence of the domain size of polycrystalline $BaTiO_3$[12,45–47] is displayed, showing classical $\sim g^{0.5}$ scaling behavior (the blue dashed line represents a fit of the data from Huan et al.[47]). b) In comparison, the domain size of polycrystalline $ErMnO_3$ decreases with increasing grain size, corresponding to inverted domain scaling behavior with $\sim g^{-0.1}$ as indicated by the fit (red dashed line; a detailed description of the determination of the median domain size is provided in Figure S9, Supporting Information).

To quantify the confinement-related variations in the domain structure, we analyze the domain size as function of the grain size. **Figure 3** displays the domain size in relation to the grain size of classical polycrystalline $BaTiO_3$ taken from the literature[12,45–47] (Figure 3a) and the polycrystalline $ErMnO_3$ samples (Figure 3b) synthesized under different heat-treatment conditions. To reliably quantify the domain size of $ErMnO_3$, we apply two different approaches, namely the maximum ball method and a stereographical method as explained in Figure S9 (Supporting Information).[48,49] Independent of the evaluation method, we find that the domain size decreases with increasing grain size; in other words, the largest grains exhibit the smallest domains. By fitting the universal scaling law ($d \sim g^m$) to the data in Figure 3b, we find an exponent $m = -0.14 \pm 0.06$ using the maximum ball method and $m = -0.10 \pm 0.07$ using the stereographic method (see Figure S9i, Supporting Information, for details). Importantly, independent of the method, we consistently observe a negative exponent m. To exclude any processing related errors, we further verify the inverted scaling behavior by manufacturing a second batch utilizing the same processing conditions as the first batch. The data show that the negative coefficient can become even smaller than –0.1 (Figure S10, Supporting Information), confirming the emergence of inverted domain scaling behavior in $ErMnO_3$. This scaling behavior is surprising as it is opposite to that known from classical polycrystalline ferroelectrics.[11,14] The latter is strikingly reflected by the comparison with the literature data for $BaTiO_3$ ($m = +0.5$) in Figure 3a.[12,45–47] The unusual domain scaling behavior in polycrystalline $ErMnO_3$ points toward a different and so far unknown origin, going beyond the domain wall related reduction of elastic energies[14] that explains the positive scaling coefficients in, e.g., $BaTiO_3$[12] and $Pb(Zr,Ti)O_3$.[11] In contrast to these materials, $ErMnO_3$ is co-elastic (not ferroelastic) and, hence, cannot simply release elastic strain by inserting or removing domain walls.[50] Note that the scaling behavior observed in our polycrystalline $ErMnO_3$ is opposite to classical Kittel scaling, which says that the domain width in thin films is inversely proportional to one over the square root of their thickness.[51]

4. Strain-Driven Unfolding of Vortex/Anti-Vortex Pairs

In order to understand the origin of the inverse grain-size-dependent domain scaling in Figure 3, we perform phase field simulations. The results are summarized in **Figure 4**. Analogous to previous studies,[16,17] the order parameter of the system is represented by a 2D vector in the basal plane of $ErMnO_3$ with magnitude Q and phase ϕ (see the Supporting Information for details). The domain size in the basal plane is determined by the competition between the strain coupling energy density of the strain fields, f_{strain}, and gradient energy density of the order parameter, f_{grad}, which are[16,17]

$$f_{strain} = \lambda Q^2 \left[(\varepsilon_{xx} - \varepsilon_{yy}) \frac{\partial \phi}{\partial x} - 2\varepsilon_{xy} \frac{\partial \phi}{\partial y} \right] \text{and} \quad (1)$$

$$f_{grad} = \frac{s_Q^x}{2} \left\{ \left(\frac{\partial Q}{\partial x} \right)^2 + \left(\frac{\partial Q}{\partial y} \right)^2 + Q^2 \left[\left(\frac{\partial \phi}{\partial x} \right)^2 + \left(\frac{\partial \phi}{\partial y} \right)^2 \right] \right\} \quad (2)$$

where λ is the strain coupling coefficient and s_Q^x is the gradient energy coefficient. As displayed in Equation (1), the strain $\varepsilon_{xx} - \varepsilon_{yy}$ favors the domain modulation along the x-direction, whereas the shear strain ε_{xy} favors domain modulation along the y-direction, both resulting in negative values of f_{strain}. Furthermore, the value of f_{strain} decreases with increasing magnitude of the phase gradients $\frac{\partial \phi}{\partial x}$ and $\frac{\partial \phi}{\partial y}$, whereas the value of f_{grad} decreases with decreasing magnitude of the phase gradients (Equation (2)). The equilibrium domain size is determined by the balance between f_{strain} and f_{grad}. When the magnitude of $\varepsilon_{xx} - \varepsilon_{yy}$ or ε_{xy} is increased, f_{strain} becomes larger, and the balance between the two energy terms results in smaller equilibrium domain sizes. This theoretical approach allows for simulating the impact of an inhomogeneous strain field described by the distribution of the shear strain components, i.e., $\varepsilon_{xx} - \varepsilon_{yy}$ and ε_{xy}.

The most pronounced strain-related feature arising from the geometrical 3D confinement in polycrystalline materials is the emergence of enhanced elastic strain at grain boundaries.[52] In our simplified strain map, we account for this feature by

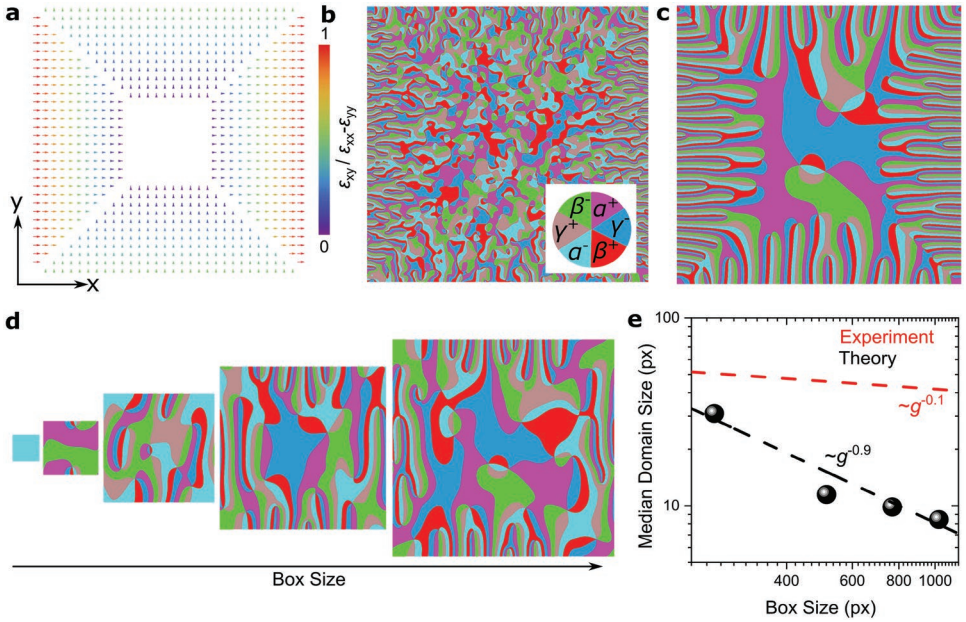

Figure 4. Interplay between elastic strain fields and vortex/anti-vortex pairs revealed by phase field simulations. a) Domain structures are simulated utilizing a gradient with enhanced elastic strain[52] near the edge of the box. b) An intermediate and c) the final domain structure are displayed. The six structural trimerization domains are labeled according to the color wheel in the inset of (b) with α^+, β^+, γ^+ corresponding to $+P$ domains and α^-, β^-, γ^- to $-P$ domains. To simulate the impact of varying grain size on the domain scaling behavior, we perform simulations with different box sizes, as displayed in (d). e) The median domain size is displayed as a function of the box size for superimposing strain fields (Figure S11, Supporting Information). The domain size continuously decreases with increasing box size following the relationship $\sim g^{-0.9}$, consistent with the experimentally observed inverted domain scaling behavior observed in our polycrystalline $ErMnO_3$ materials (Figure 3).

introducing strain gradients as displayed in Figure 4a. Figure 4b,c show representative snapshots that document how the ferroelectric domain structure evolves under the inhomogeneous strain field. Colors indicate the six structural trimerization domains in $ErMnO_3$ labeled according to the color wheel in the inset to Figure 4b with α^+, β^+, γ^+ corresponding to $+P$ domains and α^-, β^-, γ^- to $-P$ domains. A region with meandering domain walls and randomly distributed vortex/anti-vortex pairs arises in the central region of Figure 4c, corresponding to the established zero-strain ground state in hexagonal manganites.[25,40,41] The phase field simulations reveal that the elastic strain creates a pulling force on the vortex/anti-vortex pairs, unfolding the vortex domains into elongated stripe-like domains toward the boundaries with the domain walls oriented perpendicular to them. As displayed in the simulated domain structure in Figure 4c, the periodicity of the final simulated stripe-like domains is doubled along the x-direction, in comparison to the y-direction, directly following the magnitude of the elastic strain field (Figure 4a and Equation (1)). Furthermore, the simulations reveal that the relaxed domain structure forms via strain-driven annihilation of vortex/anti-vortex pairs, as well as vortex annihilation at the grain boundaries. The phase field simulations thus corroborate that the formation of the peculiar ferroelectric domain structures observed in polycrystalline $ErMnO_3$ is driven by elastic strain fields associated with the microstructural confinement.

In polycrystalline materials, elastic strains are maximized in the vicinity of the grain boundary and decay toward the center of the grain.[52] To simulate the impact of varying grain size on the domain structure, we assume that the range of the strain fields toward the center of the grain is independent of the grain size.[53] In small grains, strain fields along the x-direction (ε_{xx}) and the y-direction (ε_{yy}) overlap, whereas the area where ε_{xx} and ε_{yy} do not overlap increases for larger grains. As shown in Equation (1), the strain driving force is determined by the magnitude of $\varepsilon_{xx} - \varepsilon_{yy}$. Thus, in small grains where equally strong ε_{xx} and ε_{yy} strain fields overlap, the driving force for the unfolding of vortex/anti-vortex pairs vanishes. To test this hypothesis, we simulate the domain structures with grain-size independent strain fields. The domain structures are displayed for different box sizes in Figure 4d. Consistent with the experiments, a transition from vortex- to stripe-like domains occurs, when the grain size is decreased. This transition is driven by the annihilation of vortex/anti-vortex pairs and the motion of single vortices toward the grain boundaries. For the smallest box size, the simulations predict complete annihilation of all vortices and domain walls, leading to a single-domain state. The average domain size is displayed as a function of the box size in Figure 4e, providing a measure for the scaling behavior.

As indicated by the dashed black line, the average domain size decreases with increasing size of the simulated box, reproducing the trend observed in our experiments in Figure 3 (displayed as the dashed red line for comparison). However, we find that the negative scaling exponent extracted from the phase field simulations ($m = -0.9$) is larger than the exponent observed experimentally. Possible reasons for this discrepancy are the emergence of more complex grain-size-dependent elastic strain fields[54] and/or the presence of structural defects which can hinder the annihilation process of vortex/anti-vortex pairs. Furthermore, our simulations were done in 2D. As

the experimentally investigated planes (Figure 2) can have a nonzero inclination angle with respect to the basal plane, the 2D nature of the simulations may contribute to the discrepancy between the measured and simulated value of m and the simulated values rather represent a lower boundary, while the experimentally determined domain sizes (Figure 3) average over various inclination angles and grain orientations. We further note that the experimentally observed value can get much closer to the theoretically predicted value, as indicated by Figure S10 (Supporting Information). In summary, the simulations establish the correlation between emergent ferroelectric domain patterns and local elastic strain fields and provide a mesoscopic explanation for the anomalous grain-size-dependent domain scaling behavior in polycrystalline $ErMnO_3$, revealing the annihilation of vortex/anti-vortex pairs as the key driving force.

5. Conclusion and Outlook

Our results show that improper ferroelectric $ErMnO_3$ polycrystals exhibit inverted domain scaling behavior under 3D geometrical confinement compared to classical proper ferroelectrics, such as $BaTiO_3$[12] and $Pb(Zr,Ti)O_3$.[11] In contrast to these systems, $ErMnO_3$ is not ferroelastic and, hence, cannot minimize its elastic energy by forming new domain walls. The driving mechanism that gives rise to the established scaling behavior ($d \sim g^{0.5}$) is thus suppressed in polycrystalline $ErMnO_3$. While the origin of ferroelectricity in polycrystalline $ErMnO_3$ is the same as in single crystalline counterparts, there are additional elastic strain fields from grain-to-grain interactions[52] that strongly interact with the vortex/anti-vortex structures formed by the existing domain walls. This interaction promotes the unfolding of vortex-like domains into characteristic stripe-like domains, the annihilation of vortex/anti-vortex pairs and vortex annihilation at grain boundaries. The latter reduces the number of domains and domain walls and, hence, gives rise to the inverted domain scaling behavior. Based on our results, we expect that the inverted domain scaling behavior is not restricted to $ErMnO_3$. Possible candidate materials are non-ferroelastic systems with topological defects in their domain structure than can move and annihilate in response to elastic strain fields. Aside from the hexagonal manganites, this includes the isostructural hexagonal ferrites[55] and gallates,[56] as well as hexagonal tungsten bronzes.[57]

The substantial impact of topological defects on the grain-size-dependent domain scaling behavior is intriguing as it provides a conceptually different handle for tuning the electromechanical and dielectric performance of ferroelectric materials, giving a new dimension to, e.g., macroscopic capacitor applications[58] and domain wall based nanoelectronics.[24,27] Furthermore, recent advances in strain-field engineering utilizing dislocations,[8] secondary phases,[9] and precipitates,[10] offer an interesting playground for future confinement studies. While our discussion is centered around isotropic grains, the texturing of grains in polycrystalline materials will enable further degrees of freedom for strain engineering.[59] In general, designing polycrystals is a versatile processing-accessible path to adjust the domain structure of ferroelectrics utilizing topological defects, facilitating high tunability via strain fields, cooling rate,[28,29] and chemical doping[6] beyond the regimes accessible with single crystals and thin films.

Supporting Information

Supporting Information is available from the Wiley Online Library or from the author.

Acknowledgements

The authors acknowledge NTNU for support through the Enabling Nanotechnologies: Nano program. The Research Council of Norway is acknowledged for the support to the Norwegian Micro- and Nano-Fabrication Facility, NorFab (Project No. 245963/F50). J.S. acknowledges support from the Alexander von Humboldt Foundation through the Feodor-Lynen fellowship. J.S. and D.M. acknowledge NTNU Nano for the support through the NTNU Nano Impact fund. D.M. thanks NTNU for support through the Onsager Fellowship Program, the outstanding Academic Fellow Program, and acknowledges funding from the European Research Council (ERC) under the European Union's Horizon 2020 Research and Innovation Program (Grant Agreement No. 863691). H.W.Å. acknowledges NTNU for financial support through the NTNU Aluminium Product Innovation Center (NAPIC). The efforts on the phase-field simulations were supported by the Computational Materials Sciences Program funded by the U.S. Department of Energy, Office of Science, Basic Energy Sciences, under Award No. DE-SC0020145.

Conflict of Interest

The authors declare no conflict of interest.

Data Availability Statement

The data that support the findings of this study are available from the corresponding author upon reasonable request.

Keywords

domain engineering, improper ferroelectrics, piezoresponse force microscopy, polycrystals, topological defects

Received: April 16, 2022
Revised: August 17, 2022
Published online: October 13, 2022

[1] K. Uchino, *Ferroelectric Devices*, CRC Press, Boca Raton, FL, USA **2009**.
[2] Q. M. Zhang, H. Wang, N. Kim, L. E. Cross, *J. Appl. Phys.* **1994**, *75*, 454.
[3] D. A. Hall, *J. Mater. Sci.* **2001**, *36*, 4575.
[4] H. Lu, B. Wang, T. Li, A. Lipatov, H. Lee, A. Rajapitamahuni, R. Xu, X. Hong, S. Farokhipoor, L. W. Martin, *Nano Lett.* **2016**, *16*, 6460.
[5] G. Catalan, H. Béa, S. Fusil, M. Bibes, P. Paruch, A. Barthélémy, J. Scott, *Phys. Rev. Lett.* **2008**, *100*, 027602.
[6] E. Hassanpour, V. Wegmayr, J. Schaab, Z. Yan, E. Bourret, T. Lottermoser, M. Fiebig, D. Meier, *New J. Phys.* **2016**, *18*, 043015.

[7] Y. Li, S. Hu, Z. Liu, L. Chen, *Acta Mater.* **2002**, *50*, 395.
[8] M. Höfling, X. Zhou, L. M. Riemer, E. Bruder, B. Liu, L. Zhou, P. B. Groszewicz, F. Zhuo, B.-X. Xu, K. Durst, X. Tan, D. Damjanovic, J. Koruza, J. Rödel, *Science* **2021**, *372*, 961.
[9] L. M. Riemer, K. V. Lalitha, X. J. Jiang, N. Liu, C. Dietz, R. W. Stark, P. B. Groszewicz, G. Buntkowsky, J. Chen, S. T. Zhang, J. Rödel, J. Koruza, *Acta Mater.* **2017**, *136*, 271.
[10] C. Zhao, S. Gao, T. Yang, M. Scherer, J. Schultheiß, D. Meier, X. Tan, H.-J. Kleebe, L.-Q. Chen, J. Koruza, J. Rödel, *Adv. Mater.* **2021**, *33*, 2102421.
[11] C. A. Randall, N. Kim, J. P. Kucera, W. W. Cao, T. R. Shrout, *J. Am. Ceram. Soc.* **1998**, *81*, 677.
[12] G. Arlt, D. Hennings, G. Dewith, *J. Appl. Phys.* **1985**, *58*, 1619.
[13] J. Schultheiß, S. Checchia, H. Uršič, T. Frömling, J. Daniels, B. Malič, T. Rojac, J. Koruza, *J. Eur. Ceram. Soc.* **2020**, *40*, 3965.
[14] G. Arlt, *J. Mater. Sci.* **1990**, *25*, 2655.
[15] M. Šafránková, J. Fousek, S. Kižaev, *Czech J. Phys.* **1967**, *17*, 559.
[16] S. Artyukhin, K. T. Delaney, N. A. Spaldin, M. Mostovoy, *Nat. Mater.* **2014**, *13*, 42.
[17] F. Xue, X. Y. Wang, Y. Shi, S. W. Cheong, L. Q. Chen, *Phys. Rev. B* **2017**, *96*, 104109.
[18] X. Wang, M. Mostovoy, M. G. Han, Y. Horibe, T. Aoki, Y. Zhu, S. W. Cheong, *Phys. Rev. Lett.* **2014**, *112*, 247601.
[19] A. P. Levanyuk, D. G. Sannikov, *Sov. Phys. - Usp.* **1974**, *17*, 199.
[20] B. B. Van Aken, T. T. M. Palstra, A. Filippetti, N. A. Spaldin, *Nat. Mater.* **2004**, *3*, 164.
[21] C. J. Fennie, K. M. Rabe, *Phys. Rev. B* **2005**, *72*, 100103.
[22] M. Fiebig, T. Lottermoser, D. Meier, M. Trassin, *Nat. Rev. Mater.* **2016**, *1*, 16046.
[23] M. Lilienblum, T. Lottermoser, S. Manz, S. M. Selbach, A. Cano, M. Fiebig, *Nat. Phys.* **2015**, *11*, 1070.
[24] D. Meier, S. M. Selbach, *Nat. Rev. Mater.* **2021**, *7*, 157.
[25] D. Meier, J. Seidel, A. Cano, K. Delaney, Y. Kumagai, M. Mostovoy, N. A. Spaldin, R. Ramesh, M. Fiebig, *Nat. Mater.* **2012**, *11*, 284.
[26] W. Wu, Y. Horibe, N. Lee, S. W. Cheong, J. R. Guest, *Phys. Rev. Lett.* **2012**, *108*, 077203.
[27] J. Schultheiß, E. Lysne, L. Puntigam, E. Bourret, Z. Yan, S. Krohns, D. Meier, *Nano Lett.* **2021**, *21*, 9560.
[28] Q. N. Meier, M. Lilienblum, S. M. Griffin, K. Conder, E. Pomjakushina, Z. Yan, E. Bourret, D. Meier, F. Lichtenberg, E. K. H. Salje, N. A. Spaldin, M. Fiebig, A. Cano, *Phys. Rev. X* **2017**, *7*, 041014.
[29] S. M. Griffin, M. Lilienblum, K. T. Delaney, Y. Kumagai, M. Fiebig, N. A. Spaldin, *Phys. Rev. X* **2012**, *2*, 041022.
[30] J. Nordlander, M. Campanini, M. D. Rossell, R. Erni, Q. N. Meier, A. Cano, N. Spaldin, M. Fiebig, M. Trassin, *Nat. Commun.* **2019**, *10*, 5591.
[31] H. Pang, F. Zhang, M. Zeng, X. Gao, M. Qin, X. Lu, J. Gao, J. Dai, Q. Li, *npj Quantum Mater.* **2016**, *1*, 16015.
[32] N. Fujimura, T. Ishida, T. Yoshimura, T. Ito, *Appl. Phys. Lett.* **1996**, *69*, 1011.
[33] M. H. Harunsani, J. Li, Y. B. Qin, H. T. Tian, J. Q. Li, H. X. Yang, R. I. Walton, *Appl. Phys. Lett.* **2015**, *107*, 062905.
[34] A. Baghizadeh, J. M. Vieira, P. M. Vaghefi, M. G. Willinger, V. S. Amaral, *J. Appl. Phys.* **2017**, *122*, 044102.
[35] Q. H. Zhang, L. J. Wang, X. K. Wei, R. C. Yu, L. Gu, A. Hirata, M. W. Chen, C. Q. Jin, Y. Yao, Y. G. Wang, X. F. Duan, *Phys. Rev. B* **2012**, *85*, 020102(R).
[36] S. Remsen, B. Dabrowski, *Chem. Mater.* **2011**, *23*, 3818.
[37] B. B. Van Aken, A. Meetsma, T. T. Palstra, *Acta Crystallogr.* **2001**, *E57*, i38.
[38] J. Schultheiß, J. Schaab, D. R. Småbråten, S. H. Skjærvø, E. Bourret, Z. Yan, S. M. Selbach, D. Meier, *Appl. Phys. Lett.* **2020**, *116*, 262903.
[39] T. S. Holstad, D. M. Evans, A. Ruff, D. R. Småbråten, J. Schaab, C. Tzschaschel, Z. Yan, E. Bourret, S. M. Selbach, S. Krohns, D. Meier, *Phys. Rev. B* **2018**, *97*, 085143.
[40] T. Jungk, Á. Hoffmann, M. Fiebig, E. Soergel, *Appl. Phys. Lett.* **2010**, *97*, 012904.
[41] T. Choi, Y. Horibe, H. T. Yi, Y. J. Choi, W. D. Wu, S. W. Cheong, *Nat. Mater.* **2010**, *9*, 253.
[42] M. Tomczyk, A. M. O. R. Senos, I. M. Reaney, P. M. Vilarinho, *Scr. Mater.* **2012**, *67*, 427.
[43] R. C. DeVries, J. E. Burke, *J. Am. Ceram. Soc.* **1957**, *40*, 200.
[44] S. Tsurekawa, K. Ibaraki, K. Kawahara, T. Watanabe, *Scr. Mater.* **2007**, *56*, 577.
[45] Y. Q. Tan, J. L. Zhang, Y. Q. Wu, C. L. Wang, V. Koval, B. G. Shi, H. T. Ye, R. McKinnon, G. Viola, H. X. Yan, *Sci. Rep.* **2015**, *5*, 9953.
[46] T. Hoshina, Y. Kigoshi, S. Hatta, H. Takeda, T. Tsurumi, *Jpn. J. Appl. Phys.* **2009**, *48*, 09KC01.
[47] Y. Huan, X. H. Wang, J. Fang, L. T. Li, *J. Am. Ceram. Soc.* **2013**, *96*, 3369.
[48] C. Wang, K. Wu, G. G. Scott, A. R. Akisanya, Q. Gan, Y. Zhou, *Energy Fuels* **2020**, *34*, 82.
[49] A. Hubert, R. Schäfer, *Magnetic Domains: The Analysis of Magnetic Microstructures*, Springer Science & Business Media, Heidelberg, Germany **2008**.
[50] C. Fernandez-Posada, C. Haines, D. Evans, Z. Yan, E. Bourret, D. Meier, M. A. Carpenter, *J. Magn. Magn. Mater.* **2022**, *554*, 169277.
[51] C. Kittel, *Phys. Rev.* **1946**, *70*, 965.
[52] J. Schultheiß, L. Porz, L. K. Venkataraman, M. Höfling, C. Yildirim, P. Cook, C. Detlefs, S. Gorfman, J. Rödel, H. Simons, *Scr. Mater.* **2021**, *199*, 113878.
[53] J. Kuszyk, R. Bradt, *J. Am. Ceram. Soc.* **1973**, *56*, 420.
[54] P. F. Becher, M. V. Swain, *J. Am. Ceram. Soc.* **1992**, *75*, 493.
[55] J. A. McNulty, T. T. Tran, P. S. Halasyamani, S. J. McCartan, I. MacLaren, A. S. Gibbs, F. J. Lim, P. W. Turner, J. M. Gregg, P. Lightfoot, *Adv. Mater.* **2019**, *31*, 1903620.
[56] D. R. Småbråten, A. Nakata, D. Meier, T. Miyazaki, S. M. Selbach, *Phys. Rev. B* **2020**, *102*, 144103.
[57] K. Du, B. Gao, Y. Wang, X. Xu, J. Kim, R. Hu, F.-T. Huang, S.-W. Cheong, *npj Quantum Mater.* **2018**, *3*, 33.
[58] L. Puntigam, J. Schultheiß, A. Strinic, Z. Yan, E. Bourret, M. Altthaler, I. Kezsmarki, D. M. Evans, D. Meier, S. Krohns, *J. Appl. Phys.* **2021**, *129*, 074101.
[59] V. R. Vedula, S. J. Glass, D. M. Saylor, G. S. Rohrer, W. C. Carter, S. A. Langer, E. R. Fuller, *J. Am. Ceram. Soc.* **2001**, *84*, 2947.